Asian Journal of Chemistry; Vol. 38, No. 7 (2026), 1873-1889
ASIAN JOURNAL OF CHEMISTRY
https://doi.org/10.14233/ajchem.2026.36087

Quantum Chemical, Spectroscopic, Biological and Molecular Simulation Evaluation of *N*-(4-Methyl-2-pyridyl)acetamide as COX-2 Targeting Anti-Inflammatory Agent

V. GOKILA[1], K. KARPAGAVALLI[1,*], K. RAJU[2], R. ASWINI[1], S. SELVAKUMAR[3] and P. MANIKANDAN[4]

[1]Department of Physics, A.V.C. College (Autonomous), Mannampandal, Mayiladuthurai-609305, India
[2]Department of Physics, Easwari Engineering College (Autonomous) Ramapuram, Chennai-600089, India
[3]Department of Physics, Sri Akilandeswari Women's College, Wandiwash-604408, India
[4]Department of Physics, Arignar Anna Government Arts College, Cheyyar-604407, India

Corresponding author: E-mail: karpagam2abi@gmail.com

Received: 29 March 2026 *Accepted*: 13 June 2026 *Published online*: 3 July 2026 AJC-22413

Chronic inflammation has a major impact on the progression of many debilitating disorders such as rheumatoid arthritis, cardiovascular ailments and neurodegenerative conditions, emphasising the urgent identification of novel pharmacological agents with increased potency and reduced toxicity. This study focuses on the synthetic preparation, spectral studies and molecular modeling analysis and biological assessment of *N*-(4-Methyl-2-pyridyl)acetamide (4MPA), a nitrogen-containing heterocyclic compound with potential anti-inflammatory activity. Structural integrity was confirmed through FT-IR and Raman spectroscopic analyses. Computational investigations employing DFT demonstrated favourable electronic features including optimised geometries and well-distributed electrostatic potential surfaces. *In silico* pharmacological profiling indicated high oral bioavailability, excellent intestinal absorption (95.19%) and low skin permeability, affirming the drug-like nature of compound. Molecular docking studies showed stable interactions of 4MPA with inflammatory targets 5F19, with binding energy of -5.78 kcal/mol, respectively, corresponding inhibition constants suggesting moderate to strong affinity. These complexes were stabilised by key hydrogen bonds and hydrophobic interactions, indicative of potential pathway modulation. The compound also demonstrated acceptable pharmacokinetic properties, supporting its suitability as a drug candidate. These findings identify 4MPA as a promising anti-inflammatory agent with potential supplementary antimicrobial properties, warranting further mechanistic and optimisation studies.

Keywords: N-(4-Methyl-2-pyridyl)acetamide, Anti-inflammatory activity, Density functional theory, Molecular docking.

INTRODUCTION

Inflammation is an essential physiological response that protects the body against pathogens, tissue injury and harmful stimuli. However, persistent or dysregulated inflammation contributes to the development of numerous chronic diseases, including rheumatoid arthritis, inflammatory bowel disease, asthma, psoriasis, cardiovascular disorders, neurodegenerative diseases and cancer [1,2]. Chronic inflammatory disorders represent a major global health burden, with non-communicable diseases accounting for over 70% of worldwide deaths annually, including approximately 17.9 million deaths from cardiovascular diseases [3]. Rheumatoid arthritis affects more than 1% of the global population [4], while IBD impacts over 6.8 million individuals worldwide [5]. In addition, neuroinflammation plays a central role in Alzheimer's disease, which currently affects approximately 55 million people globally and is projected to increase substantially by 2050 [6]. Although corticosteroids, non-steroidal anti-inflammatory drugs (NSAIDs) and biologics remain the cornerstone of anti-inflammatory therapy, their long-term use is frequently associated with gastrointestinal, cardiovascular and renal toxicity, immunosuppression, limited efficacy and high treatment costs [7,8]. Consequently, the development of safer and more selective anti-inflammatory agents remains a significant therapeutic challenge.

Nitrogen-containing heterocyclic compounds, particularly pyridine derivatives, have attracted considerable attention due to their broad pharmacological activities and favourable pharmacokinetic properties. *N*-(4-Methyl-2-pyridyl)acetamide (4MPA) contains a pyridine ring substituted with an acetamide group and a methyl substituent, providing an electron-

rich aromatic framework capable of hydrogen bonding and productive interactions with biological targets involved in inflammation [9]. Previously structure-activity relationship (SAR) studies have demonstrated that 2-aminopyridine and pyridylacetamide derivatives exhibit enhanced affinity toward cyclo-oxygenase (COX) enzymes through hydrogen-bond interactions involving the carbonyl functionality [10,11]. Pharmacophore studies have further identified hydrogen-bond donor, hydrogen-bond acceptor and hydrophobic aromatic features as essential requirements for effective COX-2 inhibition, all of which are present in 4MPA [12]. Furthermore, acyl-substituted aminopyridines and *para*-methyl substituted pyridine derivatives have shown improved anti-inflammatory activity, lipophilicity and membrane permeability, while maintaining favourable drug-like properties [13]. These structural characteristics provide a strong rationale for selecting 4MPA as a lead scaffold for anti-inflammatory drug discovery.

Pyridine-based compounds are widely recognised as privileged scaffolds in medicinal chemistry due to their diverse biological activities including anti-inflammatory, analgesic, antimicrobial, anticancer and central nervous system effects [14,15]. Despite significant advances in computational drug design and quantum chemical methods, there remains a need to identify structurally simple, selective small molecules with improved safety profiles for inflammatory disorders [16-18]. Compared with clinically used COX-2 inhibitors, whose long-term administration has been associated with cardiovascular adverse effects, 4MPA offers a synthetically accessible and minimally functionalised framework that satisfies Lipinski's drug-likeness criteria while possessing structural features favourable for selective COX-2 binding.

Since chronic inflammatory diseases are frequently accompanied by microbial infections and oxidative stress, evaluation of the antimicrobial and antioxidant potential of 4MPA provides additional pharmacological relevance. Reactive oxygen species generated during inflammation further enhance COX-2 expression, making antioxidant activity a complementary property for anti-inflammatory drug candidates. Therefore, the present study investigates 4MPA through an integrated approach combining spectroscopic characterisation, density functional theory (DFT) calculations, molecular docking, pharmacokinetic prediction and biological evaluation to assess its potential as a promising anti-inflammatory lead molecule.

EXPERIMENTAL

The spectroscopic characteristics of *N*-(4-methyl-2-pyridyl)acetamide (4MPA) were thoroughly examined using a Bruker Alpha Platinum FT-IR spectrophotometer operating in the 4000-400 cm^{-1} range and a BRUKER RFS 27 FT-Raman spectrometer equipped with an Nd:YAG laser, covering the 4000-100 cm^{-1} range.

Computational methods: All theoretical investigations in this research were carried out using DFT with suitable quantum-chemical software Gaussian 09W [19]. The structural features, vibrational behaviour and electrostatic potential distribution of 4ABP were investigated through geometry optimisation, frequency calculations and MEP surface analysis at the B3LYP/6-311++G(d,p) level of theory [20-22]. The MEP surfaces, along with HOMO and LUMO energy levels, were obtained and visualised using GaussView software [23]. Optimised molecular geometries were displayed with Chemcraft [24], while vibrational assignments and potential energy distribution (PED) analysis were performed using the VEDA program [25]. The electronic properties of the compound were examined in the gas phase. Two-dimensional plots of the electron localisation function (ELF) and the localised orbital locator (LOL) and reduced density gradient (RDG) were generated using the Multiwfn package [26]. Drug-likeness characteristics were evaluated through the SwissADME web tool [27]. Protein structures related to the compound were verified using the PDBsum database and visualisation platform [28]. Furthermore, the pharmacokinetic and toxicity profiles (ADMET) of 4ABP were estimated using the pkCSM web server [29].

Molecular docking: The inhibitory potential of 4MPA against a cyclooxygenase-2 target was evaluated through molecular docking simulations, offering insights into its binding affinity and molecular interactions. The spatial configuration of the target protein (PDB code: 5F19) accessed *via* the PDB [30] and prepared for analysis by removing non-essential residues and water molecules using PyMOL [31], thereby improving structural clarity for molecular docking studies. Docking studies were conducted employing AutoDock version 4.2.6 [32]. Each ligand was docked with 100 runs and a population size of 150 employing the LGA parameter settings. The most favourable binding conformation for each protein was determined to be the most energetically favourable pose within the most populated cluster, representing the optimal binding mode [33]. Binding conformations were examined through detailed visual analysis and molecular representations generated using Discovery Studio Visualizer, offering valuable insights into protein–ligand interactions [34].

MD simulation protocol: MD simulations were performed with GROMACS 2024.3 to study the COX2_4MPA complexes [35]. The protein topology was created using the CHARMM36 force field and was solvated in a water box [36]. Ligand parameters were obtained from SwissParam [37] and ions were added to neutralise the system. After energy minimisation, we conducted a 100 ns simulation. The trajectory was analysed to examine the behaviour and interactions of complex. We used the gmx_mmpbsa package to predict the binding free energy of the ligand–protein interaction, components and evaluated parameters such as Rg, RMSD, SASA and RMSF to assess stability. The MM/PBSA calculations employed 1,000 frames from the last 100 ns, solving the Poisson-Boltzmann equation with the internal PBSA solver [38].

Antimicrobial and antioxidant activities: The antimicrobial activity of 4MPA was evaluated against selected bacterial strains *viz. Klebsiella*, *Pseudomonas aeruginosa*, *Escherichia coli*, *Streptococcus* and *Klebsiella* spp., as well as fungal strains (*Aspergillus niger*, *Mucor* and *Rhizopus* spp.) using the disc diffusion method. Sterile filter paper discs impregnated with the test compound were placed on inoculated agar plates, and antimicrobial activity was assessed by measuring the diameter of the inhibition zones.

The antioxidant activity of 4MPA was determined by the DPPH free radical scavenging assay using UV-visible spectro-

photometry. Briefly, 333 µL of 0.1 mM DPPH solution in methanol was mixed with 1 mL of 4MPA dissolved in DMSO at different concentrations and incubated at room temperature for 30 min. The absorbance was measured at 513 nm, where a decrease in absorbance indicated increased radical scavenging activity. L-Ascorbic acid (10-50 µg/mL) served as the positive control [39].

RESULTS AND DISCUSSION

Molecular geometry: A molecule attains its highest stability when it adopts the minimum-energy configuration. Therefore, structural optimisation was performed to obtain the most energetically favourable geometry by minimizing the total molecular energy [40]. In the present study, the geometry of 4MPA was optimised using DFT.

The optimised structure of 4MPA (Fig. 1) consists of C–C, C–O, C–H, C–N and N–H bonds. Among the homonuclear C–C bonds, C1–C3 exhibited the longest bond length (1.521 Å), whereas C8–C9 showed the shortest bond length (1.389 Å), reflecting differences in the local bonding environment. For the heteronuclear bonds, the N5–C5 bond displayed the maximum bond length of 1.413 Å, while the N4–H15 bond exhibited the minimum value of 1.008 Å.

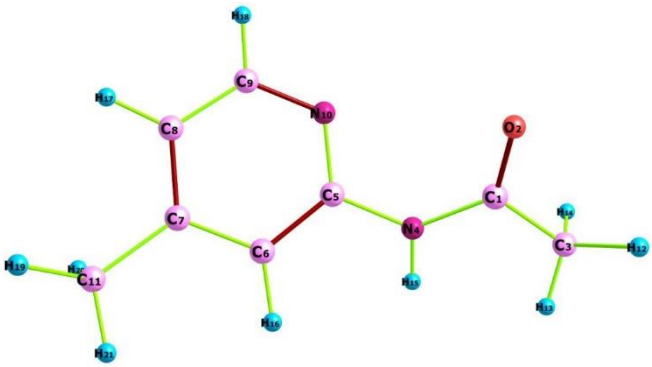

Fig. 1. Optimised molecular structure of the compound 4MPA

The calculated bond angles indicate that the molecular framework is geometrically well-defined with only minor variations. Bond angles of approximately 124º were obtained for C8–C9–N10 and O2–C1–N4, while C5–C6–H16 and C9–C8–H17 exhibited values close to 120.1º. In addition, bond angles around 108.1º were observed for C1–C3–H12, C1–C3–H14, H19–C11–H21, H12–C3–H14 and H13–C3–H14 (Table-1). These optimised structural parameters provide a reliable basis for subsequent electronic structure calculations and molecular interaction studies.

Vibration analysis: The theoretical framework predicts 57 vibrational modes for the 21-atom non-linear system based on the 3N-6 rule. Applying a 0.961 scaling factor to the DFT-calculated frequencies resulted in refined vibrational assignments [41]. Comprehensive frequency data comparing calculated and experimental values are shown in Table-2, while the experimental spectroscopic results are shown through FT-Raman and FT-IR spectra in Figs. 2 and 3.

The vibrational signature of N–H bonds in heterocyclic structures is well-known within the 3500–3000 cm^{-1} range [42,43]. Spectroscopic analysis of the target compound detected the N–H stretching mode at 3412 cm^{-1} *via* FT-IR analysis. This experimental frequency aligns well with computational predictions of 3490 cm^{-1}, with potential energy distribution analysis confirming exclusive N–H stretching character (100% PED). The presence of methyl groups introduces two asymmetric and one symmetric C-H stretching vibrations into molecular spectra. In 4MPA, the two CH_3 substituents experience significant electronic coupling with neighbouring carbonyl groups, profoundly altering the electronic structure of compound and thus affecting vibrational properties and spectral intensities [44,45]. DFT calculations predicted asymmetric stretching at 3015, 2987, 2977 and 2961 cm^{-1}, experimentally confirmed at 3010 cm^{-1} through FT-Raman spectroscopy. The symmetric stretching modes were calculated at 2918 and 2911 cm^{-1}, with experimental verification at 2927 cm^{-1} (FT-IR) and 2928 cm^{-1} (FT-Raman). The vibrational signature of aromatic C-H bonds is well-documented within the 3100-3000

TABLE-1
BOND LENGTHS AND BOND ANGLES OF 4MPA

Bond length (Å)	Values	Bond length (Å)	Values	Bond angle (º)	Values	Bond angle (º)	Values
C1-O2	1.209	C6-H16	1.085	O2-C1-C3	122.4	C5-N10-C9	117.0
C1-C3	1.521	C7-C8	1.401	O2-C1-N4	124.0	C7-C6-H16	120.5
C1-N4	1.392	C7-C11	1.507	C3-C1-N4	113.6	C6-C7-C8	117.1
C3-H12	1.089	C8-C9	1.389	C1-C3-H12	108.8	C6-C7-C11	121.6
C3-H13	1.093	C8-H17	1.084	C1-C3-H13	113.6	C8-C7-C11	121.3
C3-H14	1.094	C9-N10	1.337	C1-C3-H14	108.5	C7-C8-C9	118.9
N4-C5	1.413	C9-H18	1.086	C1-N4-C5	127.0	C7-C8-H17	120.9
N4-H15	1.008	C11-H19	1.093	C1-N4-H15	116.5	C7-C11-H19	111.0
C5-C6	1.403	C11-H20	1.095	H12-C3-H13	109.6	C7-C11-H20	110.7
C5-N10	1.328	C11-H21	1.092	H12-C3-H14	108.1	C7-C11-H21	111.6
C6-C7	1.391			H13-C3-H14	108.1	C9-C8-H17	120.1
				C5-N4-H15	115.9	C8-C9-N10	124.1
				N4-C5-C6	118.7	C8-C9-H18	120.3
				N4-C5-N10	117.9	N10-C9-H18	115.6
				C6-C5-N10	123.4	H19-C11-H20	107.2
				C5-C6-C7	119.4	H19-C11-H21	108.2
				C5-C6-H16	120.1	H20-C11-H21	107.9

TABLE-2
EXPERIMENTAL AND COMPUTATIONAL VIBRATIONAL ASSIGNMENTS

Mode	Expt. frequency		Theoretical frequency		IR intensity		Raman activity		[d]PED assignment (%)
	IR	Raman	Unscaled	Scaled[a]	Relative	Absolute[b]	Relative	Absolute[c]	
57	3412		3632	3490	24	8	87	35	ν NH 100
56	3058	3059	3178	3054	15	5	181	72	ν CH 99
55			3163	3039	11	4	86	34	ν CH 99
54			3149	3027	17	6	91	36	ν CH 100
53		3010	3137	3015	8	3	83	33	ν CH 91
52			3108	2987	16	6	57	23	ν CH 93
51			3097	2977	14	5	63	25	ν CH 99
50			3081	2961	12	4	91	36	ν CH 93
49	2927	2928	3037	2918	9	3	204	81	ν CH 92
48			3029	2911	21	7	251	100	ν CH 97
47	1760	1683	1788	1718	258	92	27	11	ν OC 70
46	1569	1570	1639	1575	202	72	28	11	β HNC 23 + ν CC 51
45	1549		1612	1549	23	8	25	10	ν CC 64
44			1536	1476	124	44	35	14	β HNC 55
43			1497	1438	282	100	9	4	β HNC 51
42			1490	1431	55	19	18	7	β HCH 70
41			1488	1430	74	26	6	2	β HCH 68
40			1485	1427	10	3	9	4	β HCH 90
39	1413	1410	1468	1410	49	17	12	5	β HCH 84
38	1378	1378	1414	1359	3	1	11	4	β HCC 90
37			1408	1353	13	5	4	2	β HNC 37 + ν CC 11
36		1300	1396	1341	34	12	4	2	β HCH 74
35	1280	1284	1334	1282	64	23	33	13	ν NC 58
34	1264		1316	1264	23	8	37	15	ν CC 45 + β HCC 20
33	1238	1242	1277	1228	2	1	5	2	ν CC 63
32	1162	1164	1223	1175	241	86	10	4	ν CC 46
31	1112	1117	1187	1141	16	6	1	1	ν CC 31 + β HCC 36
30			1133	1089	0	0	4	1	β HNC 27 + ν CC 38
29	1033		1060	1018	4	1	0	0	β HCC 81
28			1049	1008	15	5	0	0	β HCC 65
27		996	1038	998	16	6	6	2	β HCC 48
26			1009	970	26	9	5	2	τ HCCO 41
25	966		1005	966	2	1	37	15	ν CC 16 + β HCC 47
24			986	947	1	0	0	0	τ HCCN 72
23			974	936	6	2	5	2	ν CC 48
22	881		917	882	5	2	1	0	ν CC 25
21	826		873	839	3	1	0	0	τ HCCN 69
20			831	799	29	10	1	0	τ HCCN 71
19	771	773	805	773	3	1	6	2	β HCC 27 + ν CC 39
18		744	757	728	3	1	4	2	τ HNCC 79
17	683	687	701	673	1	0	6	2	β HNC 13 + ν CC 14 + β CNC 16
16	617		616	592	6	2	3	1	τ HCCO 12 + τ HCCN 68
15	553	557	581	558	4	1	1	0	τ HCCO 62
14	520	521	552	530	23	8	8	3	β CCO 51
13			521	501	4	1	6	2	β HCC 65
12	450		459	441	67	24	2	1	τ HCCN 15 + τ HCCO 23
11			455	437	30	11	6	2	τ HNCC 71
10	405		424	408	2	1	1	0	β CCN 67
9		356	344	330	0	0	1	1	ν CC 13 + β CCN 60
8		262	280	269	2	1	1	0	β HNC 14 + β CNC 28
7		228	244	234	2	1	1	1	β HNC 19 + τ HCCN 58
6			207	199	0	0	2	1	τ HCCC 78
5		107	118	113	5	2	1	1	β HNC 42 + τ HCCO 11 + τ HNCC 12
4		71	79	76	2	1	2	1	τ HCCO 76
3			67	64	3	1	1	0	τ HCCO 88
2			35	33	2	1	3	1	τ HNCC 71
1			33	32	1	0	0	0	τ HCCC 81

[a]Scaling factor: 0.961 for B3LYP/6-311++G(d,p); [b]Relative IR absorption normality intensities with highest peak absorption equal to 100; [c]Relative raman intensities normalised to 100; [d]ν-stretching, β-Bending, τ-Torsion

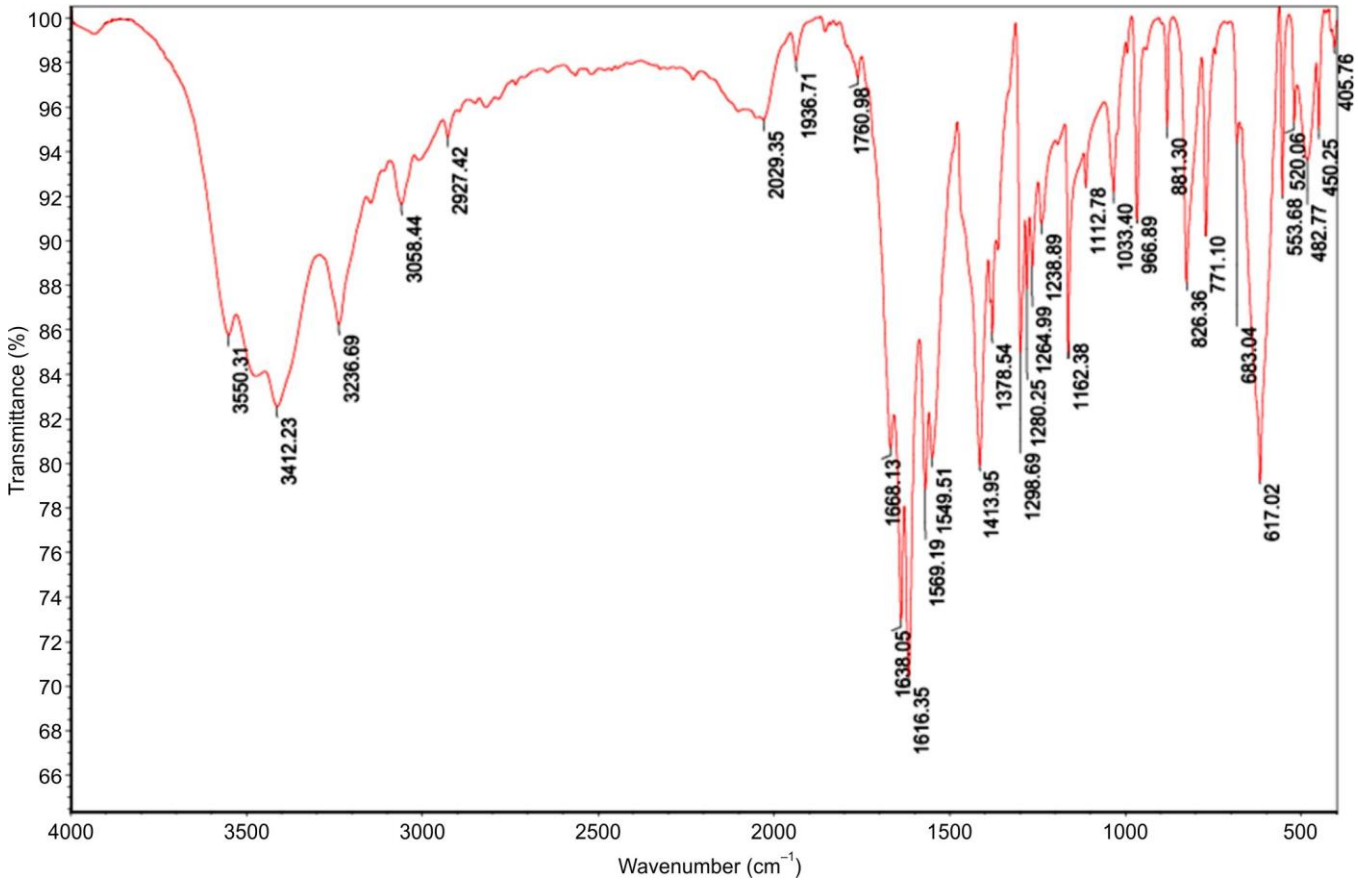

Fig. 2. Experimental FT-IR spectrum of 4MPA in 4000-400 cm^{-1} region

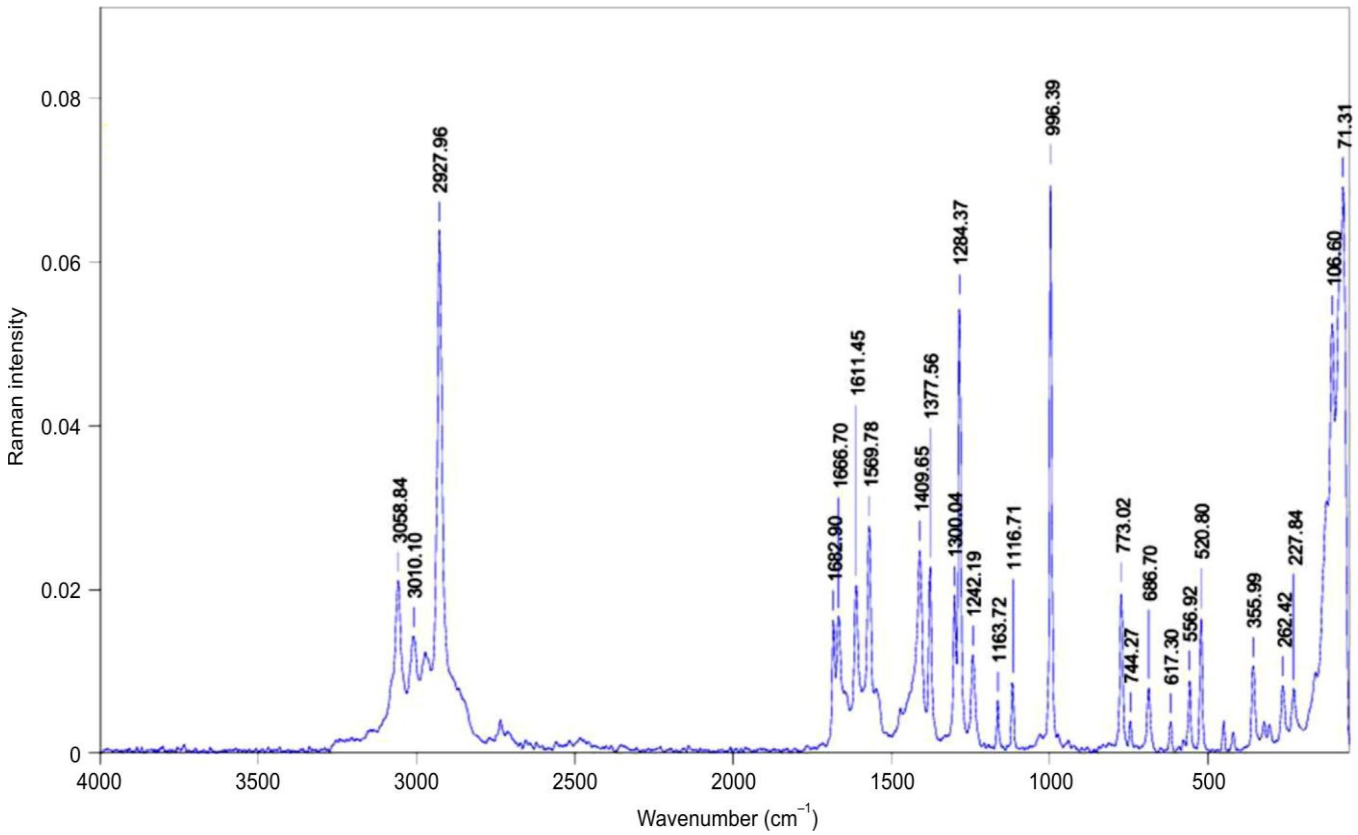

Fig. 3. Experimental FT-Raman spectrum of 4MPA in 4000-100 cm^{-1} region

cm^{-1} spectral region [46]. For the 4MPA compound, DFT calculations identified aromatic C-H stretching vibrations at 3054, 3039 and 3027 cm^{-1}. These theoretical predictions closely match experimental results, showing frequencies of 3059 cm^{-1} in FT-Raman and 3058 cm^{-1} in FT-IR analysis, confirming the accuracy of the computational assignments. Carbonyl groups show distinctive vibrational behaviour, producing strong, clear stretching modes that appear as prominent bands between 1800-1600 cm^{-1} region in infrared spectroscopy [47]. The computational analysis of 4MPA predicted the C=O stretching vibration at 1718 cm^{-1}, matching experimental frequencies of 1760 cm^{-1} (FT-IR) and 1683 cm^{-1} (FT-Raman). The C–C stretching vibrations in aromatic compounds usually occur within the 1650-1100 cm^{-1} spectral range, with exact frequencies affected by the type of ring substituents [48]. In this study, theoretical calculations predicted C–C vibrational modes at 1549, 1228, 1175, 936 and 832 cm^{-1}. The experimental results confirmed frequencies at 1549, 1238, 1162 and 881 cm^{-1} in FT-IR analysis, with additional bands at 1242 and 1164 cm^{-1} detected in FT-Raman spectroscopy. The 1350-1280 cm^{-1} region is characteristic of C–N vibrational modes; however, vibrational coupling within this region makes the unambiguous assignment of C–N stretching in the target compound challenging [49,50]. Theoretical calculations predict the C–N vibration at 1282 cm^{-1} with a 58% potential energy distribution (PED) contribution, aligning with experimental observations at 1280 cm^{-1} (FT-IR) and 1284 cm^{-1} (FT-Raman).

MESP: GaussView 6.0 were utilised to generate the 4MPA MEP map. The molecular electrostatic potential (MEP) describes the electrostatic potential generated by the molecular charge distribution at a given point surrounding the molecule [51]. In the MEP map, different colours represent variations in electrostatic potential, with red indicating regions of the most negative potential, blue representing the most positive potential and green corresponding to regions of near-neutral potential. As shown in Fig. 4, the oxygen atom is located in the red region, indicating an electron-rich site susceptible to electrophilic attack, whereas the nitrogen atom appears in the blue region, representing an electron-deficient site which is more prone to nucleophilic attack.

Fukui analysis: Fukui functions are widely used local density functional descriptors for predicting chemical reactivity and identifying molecular sites susceptible to changes in electron density during electron transfer [52,53]. The sign of Δf(r)

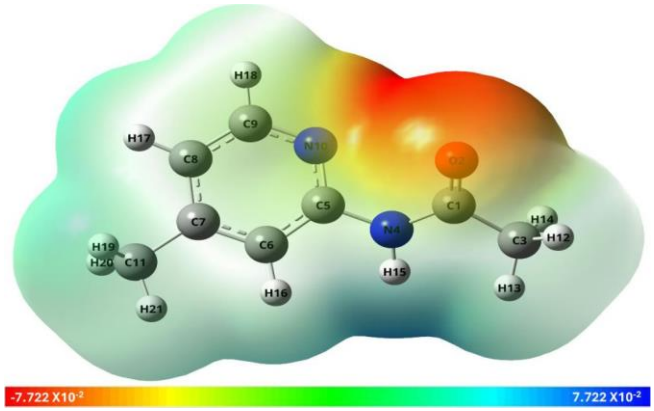

Fig. 4. Molecular electrostatic potential (MEP) map of 4MPA

distinguishes the type of reactive site: Δf(r) > 0 indicates regions prone to nucleophilic attack, whereas Δf(r) < 0 denotes sites susceptible to electrophilic attack. As summarised in Table-3, the nucleophilic centers of 4MPA are located at C3, C6 and C11, while the electrophilic centers are C1, O2, N4, C5, C7, C8, C9 and N10. These reactive sites provide valuable insight into the chemical behaviour of 4MPA during molecular interactions.

NBO analysis: Significant stabilisation energies derived from this analysis are indicative of robust chemical reactions between electron donors and acceptors [54]. Table-4 details the hyperconjugative interactions and their associated stabilisation energies. Strong π→π interactions are observed for the transitions C5–N10 (π)→C6–C7 (π) and C5–N10 (π)→C8–C9 (π), with exceptionally high second-order stabilisation energies of 192.760 and 195.440 kcal/mol, respectively. These values indicate pronounced electron delocalisation and conjugative effects within the molecular framework. Such interactions are indicative of significant stabilisation arising from extended π-conjugation, which likely enhances the resonance stability and facilitates electron delocalisation across the conjugated system. Significant lone pair (LP)→π interactions are observed for N4 (LP(1))→C5–N10 (π) and O2 (LP(2)) →C1–C3 (π), with stabilisation energies of 26.400 and 19.780 kcal/mol, respectively. These interactions highlight the involvement of non-bonding electron pairs in electron delocalisation suggesting significant n→π charge transfer contributions. This delocalisation promotes a more uniform

TABLE-3
DUAL DESCRIPTOR (FUKUI) ANALYSIS OF 4MPA

Atoms	(0,1)	(1,2)	(-1,2)	f0	f+	f–	Δf(r)
C1	0.191	0.231	0.166	-0.032	-0.040	-0.025	-0.015
O2	-0.301	-0.187	-0.336	-0.075	-0.115	-0.034	-0.081
C3	0.049	0.139	-0.191	-0.165	-0.090	-0.240	0.150
N4	0.016	0.169	-0.105	-0.137	-0.153	-0.121	-0.032
C5	0.115	0.168	0.091	-0.039	-0.053	-0.025	-0.028
C6	-0.024	0.088	-0.154	-0.121	-0.112	-0.130	0.018
C7	0.018	0.054	-0.004	-0.029	-0.036	-0.022	-0.015
C8	-0.013	0.145	-0.090	-0.117	-0.158	-0.077	-0.080
C9	0.086	0.204	0.036	-0.084	-0.117	-0.051	-0.067
N10	-0.185	-0.141	-0.204	-0.032	-0.044	-0.019	-0.026
C11	0.047	0.129	-0.210	-0.170	-0.083	-0.257	0.175

electronic distribution, leading to enhanced molecular stabilisation. Hyperconjugative stabilisation is also observed from π→σ∗ interactions, notably C5–N10 (π)→C1–N4 (σ∗) and from σ→σ∗ transitions, including C3–H14→O2–C3 (σ∗) and C6–H16→C5–N10 (σ∗). Despite their relatively modest stabilisation energies (E(2) ≈ 5-6 kcal/mol), these interactions signify crucial donor-acceptor orbital overlap, contributing to the molecule's overall stability. The increased E(2) values observed in conjugated regions suggest a high degree of electron density, rendering these sites potentially susceptible to electrophilic attack. In addition, regions exhibiting LP→π interactions are likely to function as nucleophilic centers, thereby enhancing the understanding of the chemical reactivity profile of molecule.

FMO analysis: The computed HOMO and LUMO values are -6.683 eV and -1.033 eV, respectively, giving rise to an energy gap (ΔE) of 5.650 eV (Fig. 5). This relatively wide HOMO-LUMO gap indicates that under normal environmental conditions, 4MPA shows substantial kinetic stability with low reactivity. The calculated ionisation potential (6.683 eV) and electron affinity (1.033 eV) indicate the energy required for electron removal and addition, supporting the electronic stability of 4MPA. The molecule exhibits a moderate electronegativity (3.858 eV) and a chemical potential of -3.858 eV, reflecting a balanced tendency to attract electrons. A chemical hardness of 2.825 eV and softness of 0.177 eV^{-1} further suggest low polarisability and resistance to electronic deformation, reinforcing its structural rigidity. The electrophilicity index (2.634 eV) denotes moderate electrophilic character, indicating potential reactivity toward nucleophilic sites (Table-5). Notably, the electron-donating capability (ω^- = 4.916 eV) exceeds the electron-accepting capability (ω^+ = 1.058 eV), suggesting that 4MPA functions predominantly as

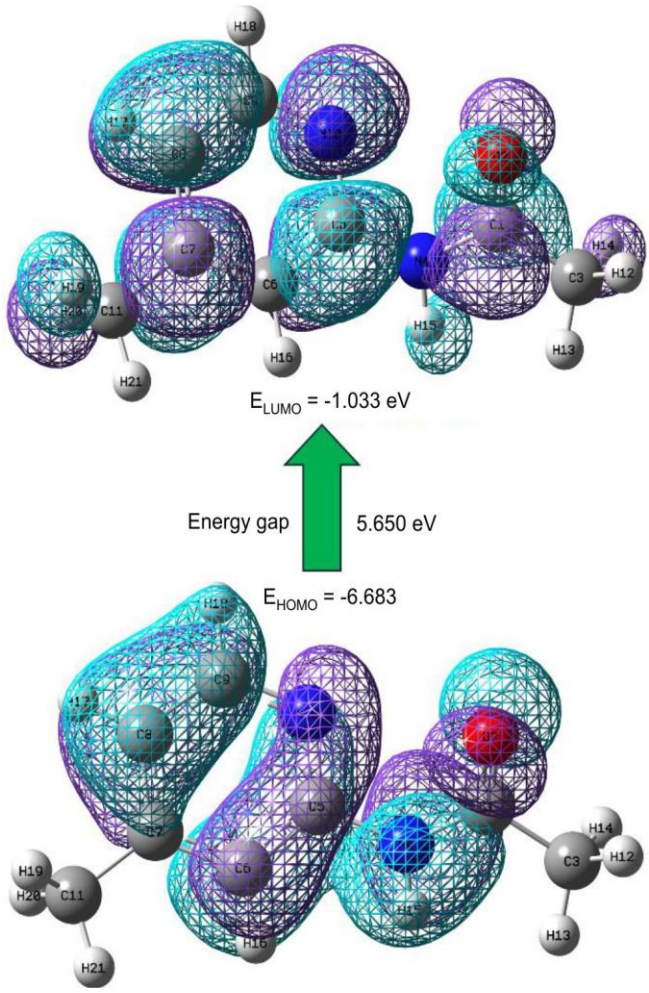

Fig. 5. HOMO-LUMO energy level diagram of 4MPA

TABLE-4
SECOND-ORDER FOCK MATRIX ANALYSIS (NBO) VALUES OF 4MPA

Donor	Type	Ed/e	Acceptor	Type	Ed/e	E(2)[a] (kcal/mol)	E(j)-E(i)[b] (a.u.)	F(i,j)[c] (a.u.)
C5-N10	π*	0.415	C6-C7	π*	0.325	192.760	0.020	0.083
C5-N10	π*	0.415	C8-C9	π*	0.295	164.740	0.020	0.080
N4	LP(1)	1.705	C1-O2	π*	0.227	43.430	0.310	0.105
C6-C7	π	1.672	C5-N10	π*	0.415	28.710	0.270	0.081
O2	LP(2)	1.855	C1-N4	σ*	0.088	28.310	0.670	0.125
C5-N10	π	1.715	C8-C9	π*	0.295	27.080	0.330	0.084
N4	LP(1)	1.705	C5-N10	π*	0.415	26.400	0.270	0.078
C8-C9	π	1.664	C6-C7	π*	0.325	25.140	0.280	0.076
O2	LP(2)	1.855	C1-C3	σ*	0.057	19.780	0.610	0.101
C8-C9	π	1.664	C5-N10	π*	0.415	15.150	0.270	0.058
C6-C7	π	1.672	C8-C9	π*	0.295	15.110	0.290	0.059
C5-N10	π	1.715	C6-C7	π*	0.325	11.370	0.330	0.055
N10	LP(1)	1.907	C5-C6	σ*	0.034	10.250	0.880	0.086
N10	LP(1)	1.907	C8-C9	σ*	0.025	8.800	0.910	0.081
C3-H14	σ	1.972	C1-O2	π*	0.227	5.240	0.560	0.051
N10	LP(1)	1.907	N4-C5	σ*	0.046	5.210	0.740	0.056
C6-H16	σ	1.979	C5-N10	σ*	0.026	4.950	1.080	0.065
C9-H18	σ	1.982	C5-N10	σ*	0.026	4.500	1.060	0.062
C11-H21	σ	1.989	C7-C8	σ*	0.024	4.480	1.080	0.062
C9-N10	σ	1.983	N4-C5	σ*	0.046	4.420	1.230	0.066

[a]$E^{(2)}$ Energy of Hyper-conjugative interaction; [b]Energy difference between donor and acceptor I and j NBO orbitals; [c]F(i,j) Fock matrix element between I and j NBO orbitals.

TABLE-5
HOMO-LUMO ENERGY VALUES AND
GLOBAL DESCRIPTOR VALUES OF 4MPA

Basis set	Gas
HOMO (eV)	-6.683
LUMO (eV)	-1.033
Ionisation potential	6.683
Electron affinity	1.033
Energy gap(eV)	5.650
Electronegativity	3.858
Chemical potential	-3.858
Chemical hardness	2.825
Chemical softness	0.177
Electrophilicity index	2.634
electronic charge	1.366
electron donating capability (ω^-)	4.916
electron accepting capability (ω^+)	1.058

an electron donor, a feature relevant for donor–acceptor systems in electronic and optoelectronic applications.

UV-Vis analysis: The UV-Visible absorption behaviour of 4MPA was investigated through both experimental measurements and theoretical TD-DFT calculations in two solvent environments gas phase and DMSO (Figs. 6 and 7). The experimental maximum absorption wavelength was recorded at 281 nm, while theoretical calculations predicted absorption at 249.364 nm in the gas phase and 252.977 nm in DMSO, corresponding to transition energies of 4.972 eV and 4.901 eV, respectively. A red shift in the absorption wavelength was observed upon solvation in DMSO, indicating stabilisation of the excited state due to solvent effects.

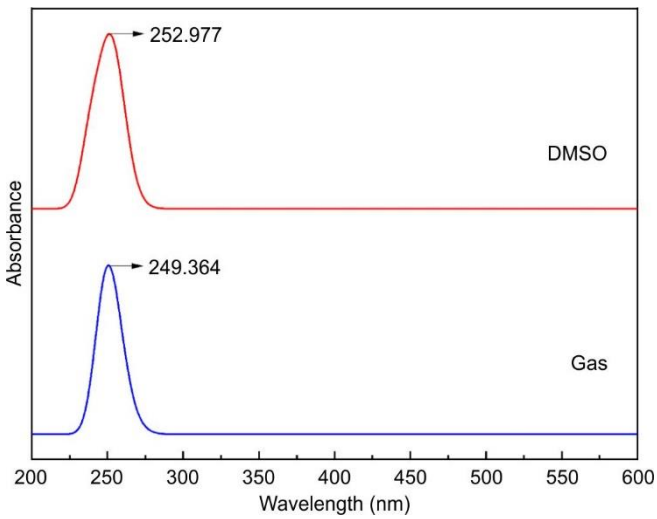

Fig. 6. UV-Vis spectra of 4MPA in gas and DMSO solvents

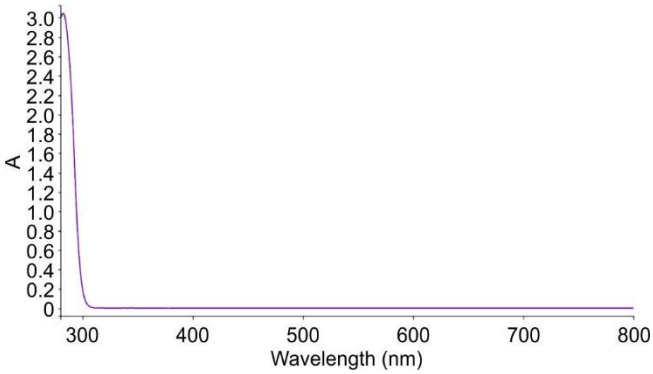

Fig. 7. Experimental UV-Vis spectrum of 4MPA in DMSO solvent

The oscillator strength, which reflects the probability of electronic transitions, increased from 0.0655 in the gas phase to 0.1227 in DMSO (Table-6). This enhancement suggests improved transition efficiency in a polar medium [55]. The light harvesting efficiency, calculated from the oscillator strength, also showed a notable increase from 13.999% to 24.612% in DMSO, indicating superior photophysical performance in polar environments. The predicted results correlate well with the experimental data and indicate the significant role of solvent polarity in modulating the electronic absorption characteristics of the compound [56].

Charge transfer analysis: The charge transfer parameters of the molecule in its first three excited states were quantitatively investigated using Multiwfn 3.8 and presented in Table-7. Key parameters such as excitation energy (E), charge transfer length (D index), Δr index and t index were calculated and analysed. This analysis highlighted the nature of the electronic excitations and the dynamics of electron-hole interactions within these excited states (Fig. 8).

The excitation energies were 4.64 eV (first excited state), 4.812 eV (second) and 4.972 eV (third), consistent with typical π–π* or n–π* transitions in conjugated systems [57]. The Dindex, measuring electron-hole separation, decreased from 2.113 Å in the first excited state to 1.733 Å (second) and 1.134 Å (third). This trend suggests a shift from long-range charge transfer in the lowest state to more localised excitations in higher states [58]. Similarly, the Δr index, also quantifying electron-hole spatial separation, decreased from 2.414 Å (first) to 1.731 Å (second) and 1.344 Å (third), reinforcing the interpretation of progressively localised excitations. The higher Δr in the first excited state points to significant intramolecular charge transfer (ICT), crucial for photovoltaic and optoelectronic applications [59]. The t index, reflecting charge transfer overlap and directionality, was positive for

TABLE-6
UV-VIS WAVELENGTHS, OSCILLATOR STRENGTH AND LHE OF 4MPA

Solvent	Energy (eV)	Expt. wavelength (nm)	Theoretical wavelength (nm)	Osc. strength	LHE (%)	Major contribs
Gas	4.972	281	249.364	0.0655	13.999	H-1->L+1 (27%), HOMO->LUMO (39%), HOMO->L+1 (10%)
DMSO	4.901	281	252.977	0.1227	24.612	H-1->LUMO (11%), HOMO->LUMO (57%), HOMO->L+1 (15%)

TABLE-7
CHARGE TRANSFER (ELECTRON-HOL) ANALYSIS OF 4MPA

Parameters	First excited state	Second excited state	Third excited state
Excitation energy E (eV)	4.64	4.812	4.972
Charge transfer length D index (Å)	2.113	1.733	1.134
Δr index (Å)	2.414	1.731	1.344
t index (Å)	0.257	0.193	-0.53

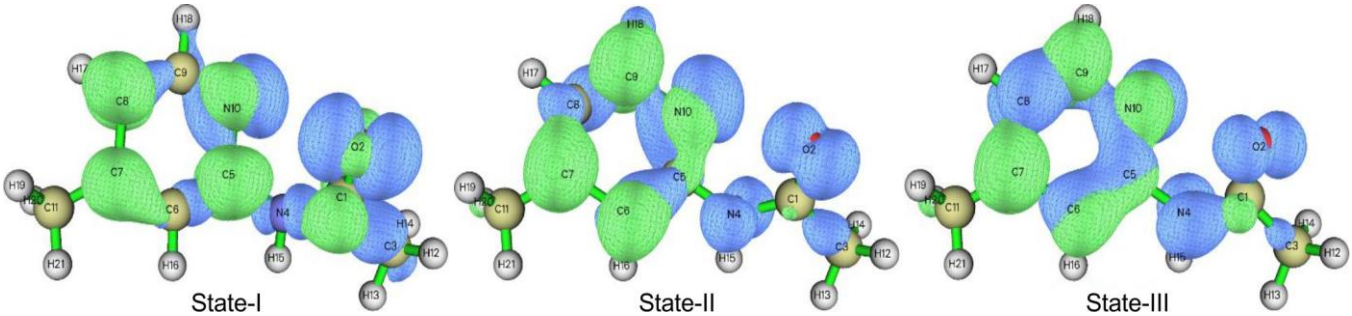

Fig. 8. Electron-Hole diagram of the first three consecutive states

the first two states (0.257 Å and 0.193 Å), indicating forward ICT. A negative t index (-0.53 Å) in the third excited state suggests a reversed or back-transfer character, aligning with localised excitation behaviour [60]. It can be inferred that the first excited state exhibits the most-strong charge transfer character, making it the most significant for photophysical processes. In contrast, the higher excited states appear to be more localised in nature.

Nonlinear optical (NLO) properties: The NLO behaviour of the compound was evaluated using DFT calculations to estimate key NLO descriptors such as dipole moment (μ), polarisability (α) and first-order hyperpolarisability (β). The molecule exhibits a total dipole moment (μ) measuring 2.041 Debye, with vector components for the x, y and z directions being -0.967 D, -1.697 D and -0.588 D, respectively [61]. This moderate dipole moment, when compared to molecules with negligible dipole moments, indicates appreciable charge separation, which plays a critical role in enhancing the molecular response to external electric fields. Comparing these components, the dipole moment is most significant along the *y*-axis, followed by the *x*-axis and is smallest along the *z*-axis. This distribution shows that the molecular charge separation is irregular across all spatial dimensions; instead, it is preferentially oriented. The molecule exhibits a mean polarisability (α) of 115.372 a.u., which translates to 1.709×10^{-23} esu. This value indicates the extent of electronic distortion experienced by the molecule in an external electric field. The anisotropy of polarisability (Δα) was calculated to be 283.949 a.u. (4.208×10^{-23} esu). The total first hyperpolarisability (β_{tot}), an important parameter for evaluating second-order NLO properties, was determined to be 133.462 a.u. (1.153×10^{-30} esu) [62]. This value significantly exceeds that of urea (0.3728×10^{-30} esu), a standard reference material, indicating that the compound exhibits a strong NLO response (Table-8). The calculated NLO parameters suggest that the title compound exhibits substantial polarisability and hyperpolarisability and the findings position the compound as a strong candidate for potential use in nonlinear optical materials and devices.

TABLE-8
NON-LINEAR OPTICAL
CHARACTERISTIC VALUES OF 4MPA

Parameter	B3LYP/ 6-311++G(d,p)	Parameter	B3LYP/ 6-311++G(d,p)
βxxx	-108.653	αxy	-1.488
βxxy	136.652	αyy	113.974
βxyy	-2.052	αxz	-1.934
βyyy	-127.447	αyz	1.523
βzxx	7.800	αzz	73.761
βxyz	0.701	α (α.u)	115.372
βzyy	-26.534	α (e.s.u)	1.709×10^{-23}
βxzz	-9.068	Δα (α.u)	283.949
βyzz	-3.350	Δα (e.s.u)	4.208×10^{-23}
βzzz	-39.853	μx	-0.967
βtot (α.u)	133.462	μy	-1.699
βtot (e.s.u)	$1.153X10^{-30}$	μz	-0.588
αxx	158.380	μ(D)	2.041

ELF & LOL: As shown in Fig. 9, the ELF map exhibits red regions around hydrogen atoms (H16, H17, H21) and covalent bond areas, signifying strong electron localisation and confirming the presence of bonding electron pairs. Yellow to green regions, particularly near carbon atoms such as C1, C6 and C7, indicate localised bonding electron density characteristic of σ-bonds in C–H and C–C interactions. In contrast, blue to violet zones represent interstitial spaces with low electron localisation. The LOL, illustrated in Fig. 10, similarly reflects electron distribution but places greater emphasis on orbital localisation. High LOL values (close to 1.0) appear as red regions around hydrogen atoms and along bonding axes, consistent with localised σ-bonding. Yellow to green regions near carbon centers suggest partial delocalisation, potentially due to π-character or conjugated systems, while outer blue to violet regions indicate nonbonding electron density or spatial voids [63].

RDG: As shown in Figs. 11 and 12, three separate interaction regions are clearly identified. The blue region at negative sign(λ_2)ρ values reveals the presence of strong

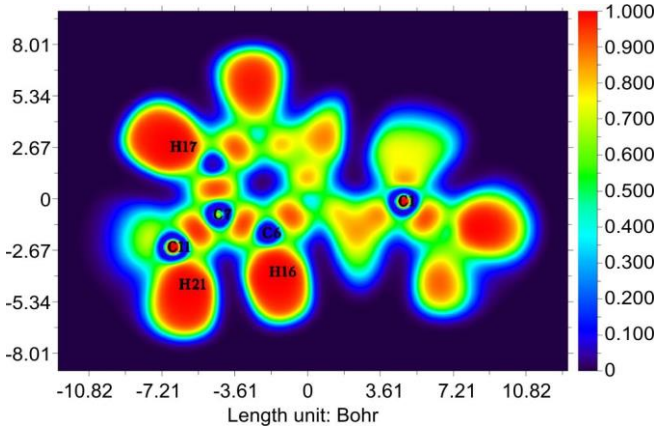

Fig. 9. Electron localisation function (ELF) of 4MPA

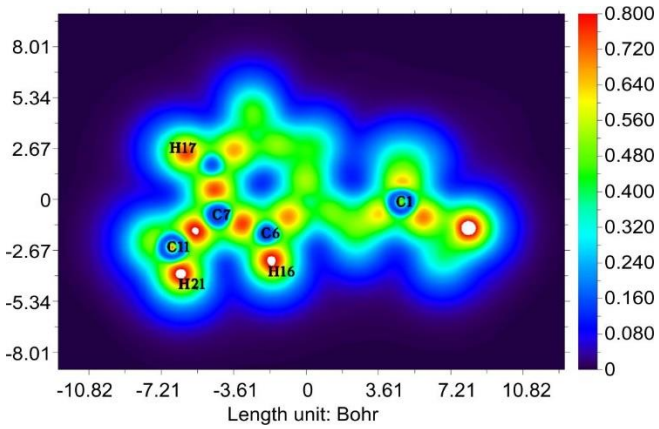

Fig. 10. Localised orbital locator (LOL) of 4MPA

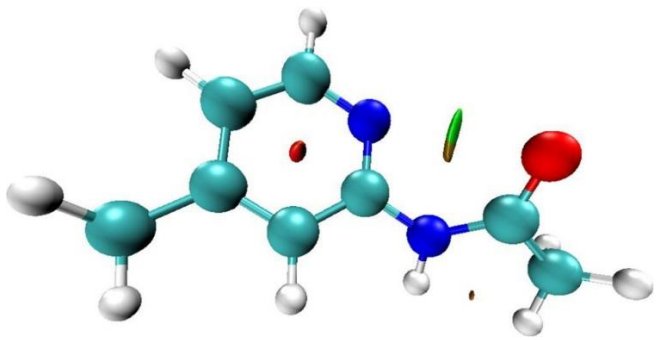

Fig. 11. RDG-NCI interaction diagram of 4MPA

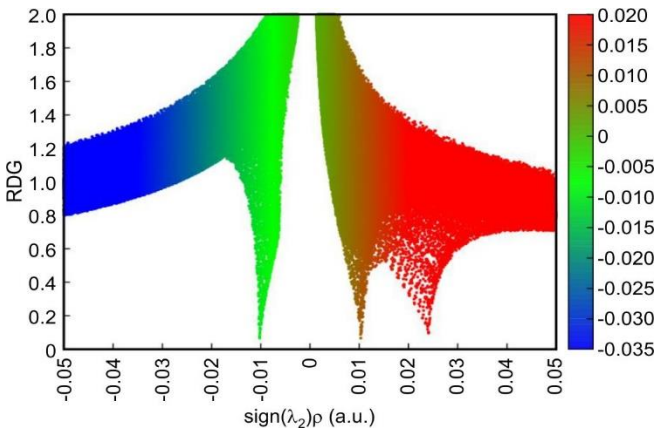

Fig. 12. RDG-2D scatter plot of 4MPA

attractive forces, likely attributed to intra- or intermolecular hydrogen bonding or dipolar interactions between donor and acceptor moieties. The green region centered around zero indicates weak dispersive interactions, typically arising from van der Waals forces and suggestive of non-bonded, spatially extended contacts, as often seen in π–π stacking and organic crystal lattices. The red region, found at positive sign(λ_2)ρ values, corresponds to repulsive interactions between closely situated electron-rich domains, indicative of steric hindrance. The pronounced green peak near the origin and the broad red spread reflect a molecular system stabilised largely by van der Waals interactions while simultaneously experiencing spatial congestion in certain areas. The presence of discrete blue spikes further confirms the evidence of directional hydrogen bonding, leading to enhanced stability of the molecular framework [64].

Drug-likeness: As presented in Table-9, the compound has a molecular weight of 150.18 g/mol, well within the threshold defined by Lipinski's rule of five (<500 g/mol), indicating promising pharmacokinetic characteristics such as absorption and permeation [65]. The presence of two rotatable bonds imparts moderate molecular flexibility, facilitating favourable conformations for biomolecular binding.

TABLE-9
DRUG-LIKENESS PARAMETERS OF 4MPA

Parameters	Values
Molecular weight	150.18 g/mol
Num. rotatable bonds	2
Num. H-bond acceptors	2
Num. H-bond donors	1
Molar refractivity	43.52
TPSA	41.99 Å^2

4MPA also possesses two hydrogen bond acceptors and one hydrogen bond donor, aligning with Lipinski's criteria (≤ 10 acceptors and ≤ 5 donors), which supports its suitability as a potential orally active drug candidate. The topological polar surface area (TPSA) of 41.99 Å^2 is considerably below the 140 Å^2 threshold, implying efficient intestinal absorption and potential to cross the blood–brain barrier. This low TPSA value is indicative of enhanced membrane permeability and bioavailability. The molar refractivity of 43.52 lies within the generally accepted range (40-130), reflecting an appropriate balance between molecular size and polarisability-factors crucial for drug-receptor interactions and solubility. These parameters affirm that 4MPA complies with the established criteria for drug-likeness and may function as a promising candidate for subsequent pharmacological and preclinical investigations.

ADMET: The ADMET properties of 4MPA, predicted using the pkCSM tool (Table-10), indicate favourable pharmacokinetic characteristics for oral drug development. The compound exhibited high human intestinal absorption (95.19%) and good Caco-2 permeability (log Papp = 1.64), suggesting efficient gastrointestinal uptake, while its low skin permeability (log Kp = -3.133) indicates limited transdermal absorption [66].

TABLE-10
ADMET PARAMETERS OF 4MPA

Property	Model name	Predicted value	Unit
Absorption	Water solubility	-0.895	Numeric (log mol/L)
Absorption	Caco2 permeability	1.64	Numeric (log Papp in 10^{-6} cm/s)
Absorption	Intestinal absorption (human)	95.193	Numeric (% Absorbed)
Absorption	Skin Permeability	-3.133	Numeric (log Kp)
Absorption	P-glycoprotein substrate	No	Categorical (Yes/No)
Absorption	P-glycoprotein I inhibitor	No	Categorical (Yes/No)
Absorption	P-glycoprotein II inhibitor	No	Categorical (Yes/No)
Distribution	VDss (human)	-0.25	Numeric (log L/kg)
Distribution	Fraction unbound	0.577	Numeric (Fu)
Distribution	BBB permeability	-0.25	Numeric (log BB)
Distribution	CNS permeability	-2.886	Numeric (log PS)
Metabolism	CYP2D6 substrate	No	Categorical (Yes/No)
Metabolism	CYP3A4 substrate	No	Categorical (Yes/No)
Metabolism	CYP1A2 inhibitior	No	Categorical (Yes/No)
Metabolism	CYP2C19 inhibitior	No	Categorical (Yes/No)
Metabolism	CYP2C9 inhibitior	No	Categorical (Yes/No)
Metabolism	CYP2D6 inhibitior	No	Categorical (Yes/No)
Metabolism	CYP3A4 inhibitior	No	Categorical (Yes/No)
Excretion	Total Clearance	0.565	Numeric (log mL/min/kg)
Excretion	Renal OCT2 substrate	No	Categorical (Yes/No)
Toxicity	AMES toxicity	No	Categorical (Yes/No)
Toxicity	Max. tolerated dose (human)	1.195	Numeric (log mg/kg/day)
Toxicity	hERG I inhibitor	No	Categorical (Yes/No)
Toxicity	hERG II inhibitor	No	Categorical (Yes/No)
Toxicity	Oral rat acute toxicity (LD_{50})	2.347	Numeric (mol/kg)
Toxicity	Oral rat chronic toxicity (LOAEL)	2.475	Numeric (log mg/kg_bw/day)
Toxicity	Hepatotoxicity	Yes	Categorical (Yes/No)
Toxicity	Skin sensitisation	No	Categorical (Yes/No)
Toxicity	*T. pyriformis* toxicity	-0.277	Numeric (log ug/L)
Toxicity	Minnow toxicity	2.1	Numeric (log mM)

The compound exhibited moderate to low predicted water solubility, indicating that formulation optimisation may be required to improve bioavailability. It showed moderate distribution (log VDss = -0.25) with a high unbound plasma fraction (Fu = 0.577). Low BBB (log BB = -0.25) and CNS permeability (log PS = -2.886) suggest limited central nervous system exposure, reducing the likelihood of CNS-related adverse effects [67]. Metabolic predictions indicated that 4MPA is neither a substrate nor an inhibitor of major CYP450 isoenzymes, suggesting low potential for drug–drug interactions and good metabolic stability [68]. The compound also exhibited moderate total clearance (log CL = 0.565) and no interaction with renal OCT2 transporters, indicating elimination primarily through hepatic metabolism and passive renal filtration [69]. Toxicity assessment predicted negative AMES mutagenicity, no hERG I/II inhibition and no skin sensitisation, although potential hepatotoxicity warrants further *in vivo* investigation. Thus, the favourable ADMET profile supports the potential of 4MPA as an oral drug candidate; however, experimental validation is required to confirm these *in silico* predictions [70].

Molecular docking: Cyclooxygenase-2 (COX-2; PDB ID: 5F19) was selected as the docking target since it is the principal inducible enzyme responsible for prostaglandin biosynthesis during inflammation, making it an established target for anti-inflammatory therapy [71,72]. The crystal structure of aspirin-acetylated COX-2 (5F19) was chosen owing to its high stereochemical quality, with 90.7% of residues located in the Ramachandran favoured region and 9.1% in the allowed region (Fig. 13), confirming the suitability of the protein model for docking studies [73].

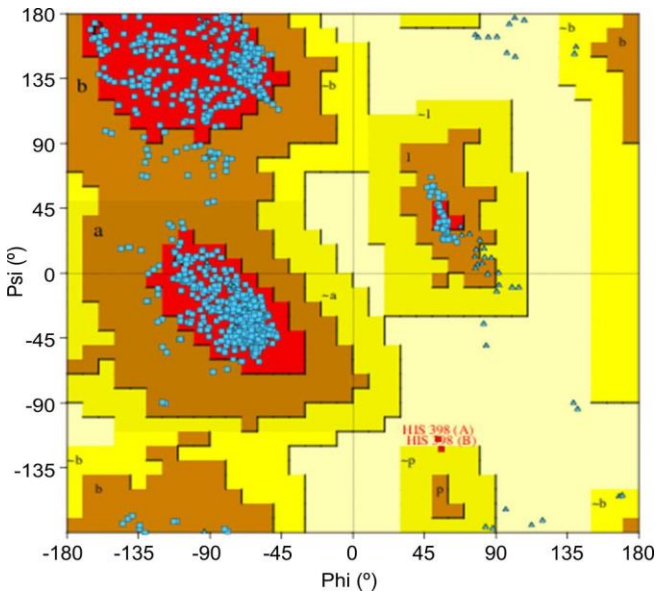

Fig. 13. Ramachandran plot for COX2 protein 5F19

The docking analysis revealed that 4MPA binds favourably within the COX-2 active site (Fig. 14), with a binding energy of -5.78 kcal/mol, intermolecular energy of -6.08 kcal/mol and a predicted inhibition constant (K_i) of 57.85 μM (Table-11). The ligand was stabilised primarily through conventional hydrogen bonds with HIS193 (2.12 Å) and THR192 (2.10 Å) involving the carbonyl and amide groups. Additional stabilisation was provided by a π–σ interaction between the pyridine ring and ALA188 (3.91 Å), together with a hydrophobic alkyl interaction involving LEU377 (5.10 Å). These hydrogen-bonding, aromatic and hydrophobic interactions indicate favourable accommodation of 4MPA within the COX-2 binding pocket.

For comparison, the reference COX-2 inhibitor celecoxib was docked under identical conditions (Fig. 15). Celecoxib exhibited stronger binding, with a binding energy of -8.10 kcal/mol, intermolecular energy of -9.59 kcal/mol and a K_i of 1.16 μM. Its higher affinity resulted from an extensive interaction network comprising hydrogen bonds, π–π stacking, π-cation, π-sulphur and hydrophobic contacts involving residues ASN-368, HIS372, HIS374, HIS193, TRP373, ALA188, VAL430, LEU376 and LEU377. Although 4MPA displayed lower binding affinity than celecoxib, it interacted with key active-site residues, particularly HIS193 and ALA188, confirming effective engagement with the COX-2 binding pocket. These findings demonstrate that the pyridine–amide scaffold of 4MPA

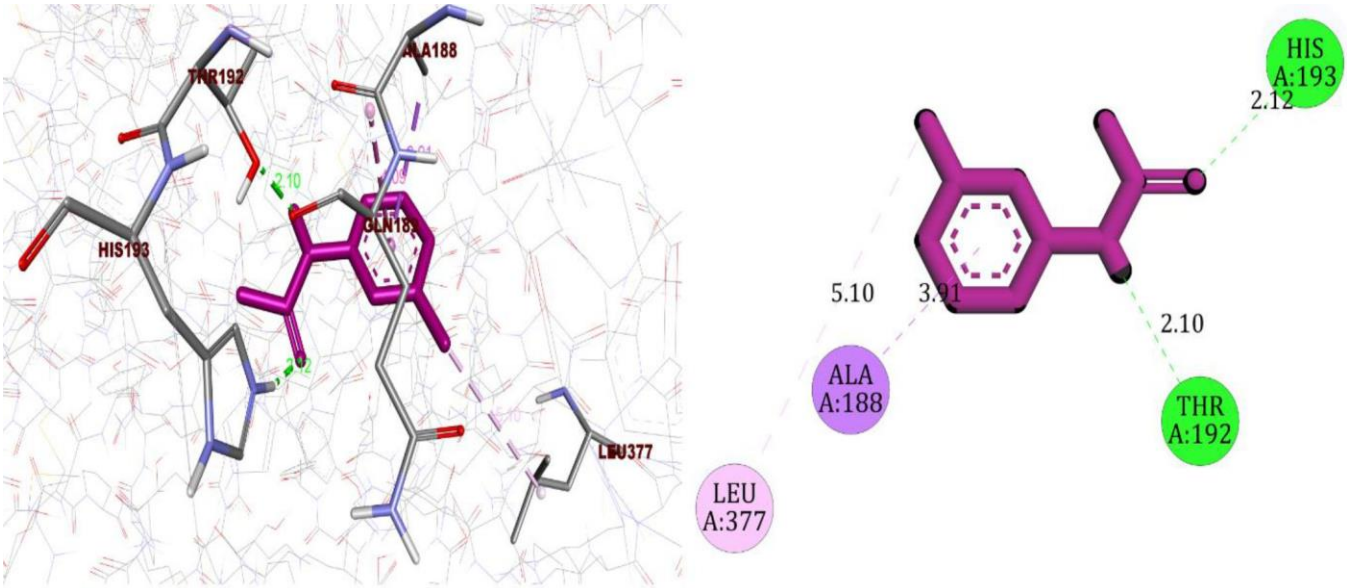

Fig. 14. Molecular docking interaction for 3D and 2D of 4MPA with COX2 receptor

TABLE-11
PROTEIN-LIGAND BINDING ENERGY, BONDED RESIDUES AND INTERACTION DETAILS

Protein (PDB)	Ligand	Binding energy (kcal/mol)	Intermolecular energy (kcal/mol)	Inhibition constant (μm)	Protein residues	Ligand groups	*Type	Distance (Å)
5F19	4MPA	-5.78	-6.08	57.85	HIS193	CO	COHB	2.12
					THR192	NH	COHB	2.1
					ALA188	Ring	PS	3.91
					LEU377	CH	AL	5.1
	Celecoxib (standard drug)	-8.1	-9.59	1.16	ASN368	NH	COHB	2.12
					ASN368	NH	COHB	2.19
					HIS372	CS	PS	3.99
					HIS372	Ring	PPS	5.12
					LEU376	CH	AL	4.3
					TRP373	CH	PAL	4.61
					ALA188	CH	AL	3.25
					ALA188	Ring	PAL	5.25
					HIS374	Ring	PPTS	5.47
					HIS374	CF	PAL	5.46
					VAL430	CF	AL	5.29
					HIS193	Ring	PC	2.27
					LEU377	CF	AL	4.44

*COHB - Conventional hydrogen bond; PS-π-Sigma; AL-Alkyl: PAL - π Alkyl; PS - π Sulfur; PPS - π π Stacked; PPTS - π π T Shaped; PC - π Cation

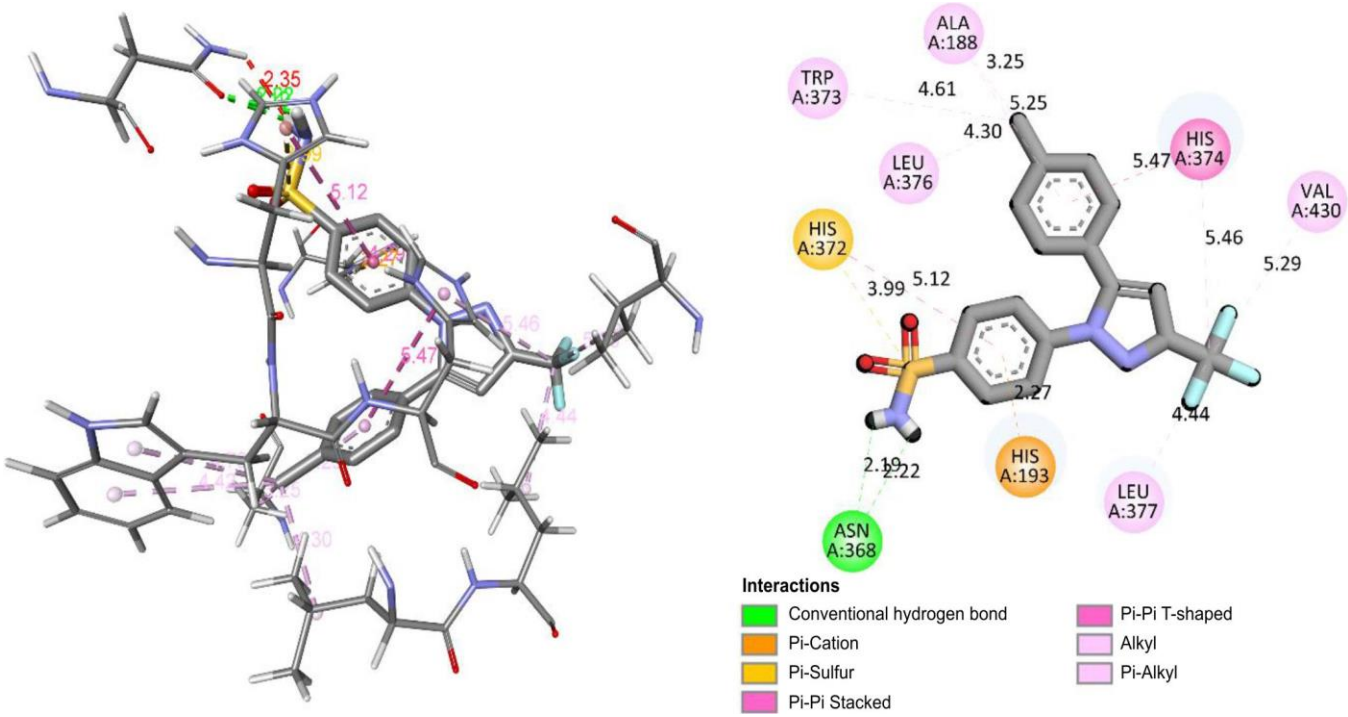

Fig. 15. Molecular docking interaction for 3D and 2D of celecoxib (standard drug) with COX2 receptor

possesses the essential pharmacophoric features required for COX-2 recognition and represents a promising lead for further structural optimisation to enhance anti-inflammatory activity.

Molecular dynamics simulation: Molecular dynamics (MD) simulations were performed to evaluate the structural stability and dynamic behaviour of the COX-2–4MPA complex under physiological conditions, complementing the molecular docking results. The root means square fluctuation (RMSF) profile (Fig. 16) showed that most residues fluctuated below 0.20 nm, indicating minimal structural deviations throughout the simulation [74]. Slightly higher fluctuations were observed in the N-terminal region (residues 20-100) and flexible loop regions (170-200 and 480-520), whereas the active-site residues remained stable. The maximum fluctuation (~0.40 nm) occurred near the N-terminus, while the core and C-terminal domains exhibited lower fluctuations (0.10-0.15 nm), demonstrating that 4MPA binding maintained overall protein stability with only localised flexibility.

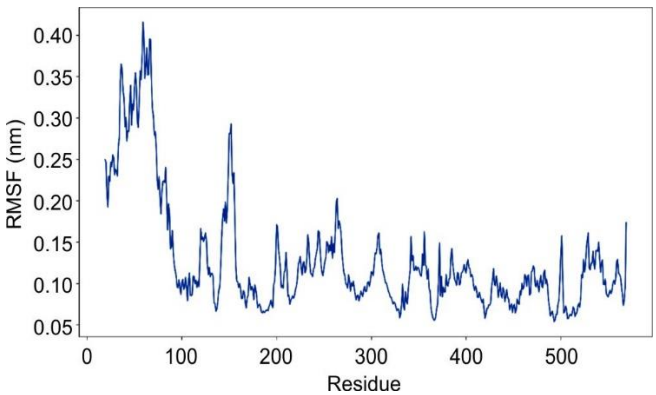

Fig. 16. Molecular dynamics simulation of RMSF for 4MPA-COX2 receptor over 100 ns

The root mean square deviation (RMSD) trajectory (Fig. 17) further confirmed complex stability [75]. Following an initial equilibration phase during the first 10 ns, the RMSD reached approximately 0.25 nm and subsequently remained stable between 0.22 and 0.30 nm throughout the 100 ns simulation, indicating that ligand binding did not induce significant conformational changes in the COX-2 structure.

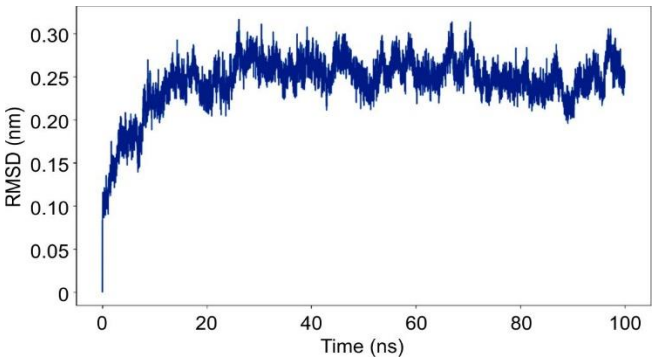

Fig. 17. Molecular dynamics simulation of RMSD for 4MPA-COX2 receptor over 100 ns

The solvent-accessible surface area (SASA) profile (Fig. 18) fluctuated only slightly between 250 and 265 nm^2, indicating that the complex retained a compact structure during the simulation [76]. Similarly, the radius of gyration (Rg) (Fig. 19) remained nearly constant (2.44-2.49 nm) after initial equilibration, confirming the preservation of protein compactness and folding [77]. The combined RMSF, RMSD, SASA and Rg analyses demonstrate that 4MPA forms a stable COX-2 complex with sustained hydrogen-bonding and hydrophobic interactions, supporting its favourable binding mode and conformational stability throughout the simulation.

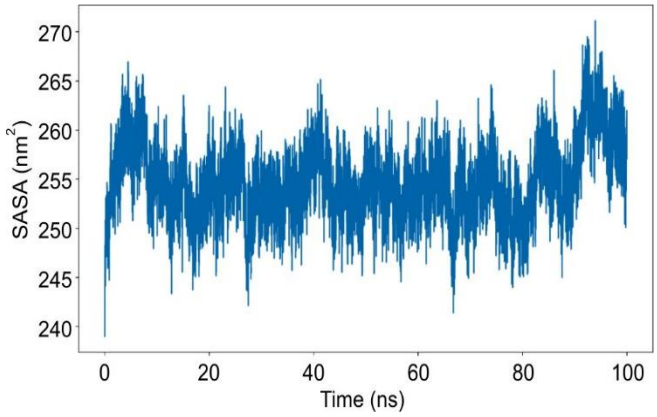

Fig. 18. SASA plot of 4MPA with COX2 receptor over 100 ns simulation

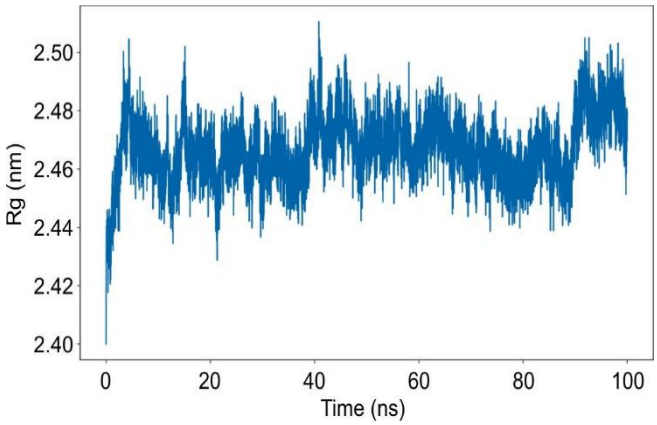

Fig. 19. Radius of gyration (Rg) of 4MPA with COX2 complex over 100 ns simulation

Binding free energy: The binding affinity of the COX2-4MPA was estimated using the MM/PBSA approach [78]. The binding free energy components obtained from the MM/GBSA analysis are presented in Table-12. The total binding free energy (ΔG_{total}) of -17.64 kcal/mol indicates a spontaneous and energetically favourable ligand–receptor interaction. The van der Waals energy (ΔV_{DWAALS} = -20.15 kcal/mol) was the major stabilizing factor, reflecting the importance of hydrophobic and dispersion forces in complex stabilisation.

The electrostatic interaction energy (ΔE_{EL} = -13.63 kcal/mol) contributed favourably, emphasizing the role of electrostatic attractions between the ligand and active-site residues. Together, these terms yield a gas-phase energy (ΔG_{GAS}) of -33.78 kcal/mol, representing the principal driving force for binding. In contrast, the solvation free energy (ΔG_{SOLV} = 16.14 kcal/mol), comprising polar (ΔE_{GB} = 19.50 kcal/mol) and non-polar (ΔE_{SURF} = -3.36 kcal/mol) components, partially counteracted these interactions. The negative ΔG_{total} demonstrates that favourable van der Waals and electrostatic interactions overcome the desolvation penalty, resulting in a stable protein–ligand complex.

Antimicrobial activity: Given that oxidative stress and microbial infections can aggravate inflammation through NF-κB activation and COX-2 upregulation, the antimicrobial activity of 4MPA was evaluated using the disc diffusion method [79]. Against four clinically relevant bacterial strains, 4MPA exhibited moderate antibacterial activity, with inhibition zones of 16 ± 0.5 mm for *Klebsiella*, 13 ± 0.5 mm for *Escherichia coli*, 12 ± 0.5 mm for *Streptococcus* and 10 ± 0.5 mm for *Pseudomonas aeruginosa* (Table-13). Although ciprofloxacin produced larger inhibition zones (14-18 ± 0.5 mm) [80], the activity of 4MPA, particularly against *Klebsiella* and *E. coli*, highlights its potential as a lead antibacterial scaffold. The comparatively lower activity against *P. aeruginosa* is likely due to its intrinsic resistance and low outer-membrane permeability.

In contrast, 4MPA displayed negligible antifungal activity against *Aspergillus niger*, *Mucor* and *Rhizopus*, with inhibition zones of 0.7 ± 0.1, 0.5 ± 0.2 and 0.3 ± 0.2 mm, respectively, whereas amphotericin B produced inhibition zones of 18-19 ± 0.5 mm [81]. These findings indicate that 4MPA possesses moderate antibacterial but poor antifungal activity, suggesting that structural optimisation is required to broaden its antimicrobial spectrum while preserving its antibacterial potential.

Antioxidant activity: The antioxidant activity of 4MPA was evaluated using the DPPH radical scavenging assay and the results are presented in Table-14. Both 4MPA and the reference standard (L-ascorbic acid) exhibited concentration-dependent scavenging activity over the range of 20-100 μg/mL. At 100 μg/mL, L-ascorbic acid achieved approximately 80% inhibition, whereas 4MPA showed 42% scavenging activity, indicating moderate antioxidant potential. The increasing scavenging activity with concentration suggests that 4MPA can donate hydrogen atoms or electrons to neutralize DPPH

TABLE-12
MM/PBSA BINDING ENERGY VALUES OF 4MPA-COX2 COMPLEX THROUGH MD SIMULATION

van der Waals interaction energy (ΔVDWAALS) (kcal/mol)	Electrostatic interaction energy (ΔEEL) (kcal/mol)	Polar solvation energy (ΔEGB) (kcal/mol)	Non-polar solvation energy (ΔESURF) (kcal/mol)	Gas-phase energy (ΔGGAS) (kcal/mol)	Solvation energy (ΔGSOLV) (kcal/mol)	Total binding free energy (ΔGTOTAL) (kcal/mol)
-20.15	-13.63	19.5	-3.36	-33.78	16.14	-17.64

TABLE-13
ANTIMICROBIAL VALUES OF 4MPA WITH DIFFERENT SPECIES

Multi drug resistant	4MPA	Amphotericin B	Bacteria	4MPA	Ciproflaxin
Aspergillus niger	0.7 ± 0.1	18 ± 0.5	*Streptococcus*	12 ± 0.5	16 ± 0.5
Mucor	0.5 ± 0.2	19 ± 0.5	*Klebsiella*	16 ± 0.5	18 ± 0.5
Rhizopus	0.3 ± 0.2	15 ± 0.5	*E. coli*	13 ± 0.5	14 ± 0.5

TABLE-14
DPPH ANTIOXIDANT ASSAY OF
4MPA WITH VARIOUS CONCENTRATIONS

Concentration (µg)	DPPH		IC_{50}
	Standard (ascorbic acid)	4MPA	
20	17.532	43.126	
40	23.737	51.664	
60	30.159	62.301	36.1
80	36.075	72.576	
100	42.929	80.680	

radicals, thereby reducing the absorbance at 513 nm. Although less potent than the standard, the results demonstrate that 4MPA possesses concentration-dependent antioxidant activity, supporting its potential as an antioxidant lead compound [82].

Conclusion

This multidisciplinary study comprehensively characterised the novel compound N-(4-methyl-2-pyridyl)acetamide (4MPA) using spectroscopic, computational and biological methods, demonstrating its potential as an anti-inflammatory agent. Spectroscopic analyses confirmed its structural integrity, while DFT calculations revealed favourable electronic properties that support its molecular stability and chemical reactivity. The optimised electronic structure, appropriate excitation energies and charge-transfer characteristics indicate efficient electronic transitions, which may facilitate interactions with biological targets. Furthermore, the moderate dipole moment and favourable molecular polarisability suggest desirable solubility and membrane permeability, supporting the drug-like nature of the compound. *In silico* pharmacokinetic analysis predicted high oral bioavailability, excellent intestinal absorption, and a low likelihood of off-target effects, indicating favourable ADMET characteristics. Molecular docking and molecular dynamics simulations further demonstrated stable binding of 4MPA within the COX-2 (5F19) active site through hydrogen-bonding and hydrophobic interactions, confirming the stability of the protein–ligand complex and supporting its potential to modulate inflammatory pathways. In addition to its anti-inflammatory potential, 4MPA exhibited moderate antibacterial activity, particularly against *Klebsiella* and *E. coli*, along with concentration-dependent antioxidant activity, achieving 42% DPPH radical scavenging at 100 µg/mL. Since oxidative stress is known to enhance COX-2 expression during inflammation, the antioxidant activity of 4MPA complements its predicted anti-inflammatory mechanism, highlighting its multifunctional pharmacological potential. Thus, the favourable structural, pharmacokinetic and biological properties of 4MPA identify it as a promising lead scaffold for further mechanistic studies, structural optimisation and *in vivo* evaluation toward the development of safe and effective anti-inflammatory therapeutics.

CONFLICT OF INTEREST

The authors declare that there is no conflict of interests regarding the publication of this article.

DECLARATION OF AI-ASSISTED TECHNOLOGIES

During the preparation of this manuscript, the authors used an AI-assisted tool(s) to improve the language. The authors reviewed and edited the content and take full responsibility for the published work.

REFERENCES

1. R. Medzhitov, *Nature*, **454**, 428 (2008); https://doi.org/10.1038/nature07201
2. L. Chen, H. Deng, H. Cui, J. Fang, Z. Zuo, J. Deng, Y. Li, X. Wang and L. Zhao, *Oncotarget*, **9**, 7204 (2018); https://doi.org/10.18632/oncotarget.23208
3. World Health Organisation (WHO), Noncommunicable Diseases (2021); https://www.who.int/news-room/fact-sheets/detail/noncommunicable-diseases
4. G.S. Firestein and I.B. McInnes, *Immunity*, **46**, 183 (2017); https://doi.org/10.1016/j.immuni.2017.02.006
5. S. Alatab, S.G. Sepanlou, K. Ikuta, H. Vahedi, C. Bisignano, S. Safiri, A. Sadeghi, M.R. Nixon, A. Abdoli, H. Abolhassani, V. Alipour, M.A.H. Almadi, A. Almasi-Hashiani, A. Anushiravani, J. Arabloo, S. Atique, A. Awasthi, A. Badawi, A.A.A. Baig, N. Bhala, A. Bijani, A. Biondi, A.M. Borzì, K.E. Burke, F. Carvalho, A. Daryani, M. Dubey, A. Eftekhari, E. Fernandes, J.C. Fernandes, F. Fischer, A. Haj-Mirzaian, A. Haj-Mirzaian, A. Hasanzadeh, M. Hashemian, S.I. Hay, C.L. Hoang, M. Househ, O.S. Ilesanmi, N. Jafari Balalami, S.L. James, A.P. Kengne, M.M. Malekzadeh, S. Merat, T.J. Meretoja, T. Mestrovic, H. Mirzaei, E.M. Mirrakhimov, K.A. Mohammad, A.H. Mokdad, L. Monasta, I. Negoi, T.H. Nguyen, C.T. Nguyen, A. Pourshams, H. Poustchi, M. Rabiee, N. Rabiee, K. Ramezanzadeh, D.L. Rawaf, S. Rawaf, N. Rezaei, S.R. Robinson, L. Ronfani, S. Saxena, M. Sepehrimanesh, M.A. Shaikh, Z. Sharafi, M. Sharif, S. Siabani, A.R. Sima, J.A. Singh, A. Soheili, R. Sotoudehmanesh, H.A.R. Suleria, B.E. Tesfay, B. Tran, D. Tsoi, M. Vacante, A.B. Wondmieneh, A. Zarghi, Z.-J. Zhang, R. Malekzadeh, M. Dirac and M. Naghavi, *Lancet Gastroenterol. Hepatol.*, **5**, 17 (2020); https://doi.org/10.1016/S2468-1253(19)30333-4
6. M.T. Heneka, W.M. van der Flier, F. Jessen, J. Hoozemanns, D.R. Thal, D. Boche, F. Brosseron, C. Teunissen, H. Zetterberg, A.H. Jacobs, P. Edison, A. Ramirez, C. Cruchaga, J.-C. Lambert, A. Ruiz-Laza, J.V. Sanchez-Mut, A. Fischer, S. Castro-Gomez, T.D. Stein, L. Kleineidam, M. Wagner, J.J. Neher, C. Cunningham, S.K. Singhrao, M. Prinz, C.K. Glass, J.C.M. Schlachetzki, O. Butovsky, K. Kleemann, P.L. De Jager, H. Scheiblich, G.C. Brown, G. Landreth, M. Moutinho, J. Grutzendler, D. Gomez-Nicola, R.M. McManus, K. Andreasson, C. Ising, D. Karabag, D.J. Baker, S.A. Liddelow, A. Verkhratsky, M. Tansey, A. Monsonego, L. Aigner, G. Dorothée, K.-A. Nave, M. Simons, G. Constantin, N. Rosenzweig, A. Pascual, G.C. Petzold, C. Venegas, J. Kipnis, M. Colonna, J. Walter, A.J. Tenner, M.K. O'Banion, J.R. Steinert, D.L. Feinstein, M. Sastre, K. Bhaskar, S. Hong, D.P. Schafer, T. Golde, R.M. Ransohoff, D. Morgan, J. Breitner, R. Mancuso and S.-P. Riechers, *Nature Rev. Immunol.*, **25**, 321 (2025); https://doi.org/10.1038/s41577-024-01104-7
7. J.R. Vane and R.M. Botting, *Int. J. Tissue React.*, **20**, 3 (1998).
8. J.A. Singh, K.G. Saag, S.L. Bridges Jr., E.A. Akl, R.R. Bannuru, M.C. Sullivan, E. Vaysbrot, C. McNaughton, M. Osani, R.H. Shmerling, J.R. Curtis, D.E. Furst, D. Parks, A. Kavanaugh, J. O'Dell, C. King, A. Leong, E.L. Matteson, J.T. Schousboe, B. Drevlow, S. Ginsberg, J. Grober, E.W. St. Clair, E. Tindall, A.S. Miller and T. McAlindon, *Arthritis Rheumatol.*, **68**, 1 (2016); https://doi.org/10.1002/art.39480
9. P. Rani, D.K. Pal, R.R. Hegde and S.R. Hashim, *Hem. Ind.*, **69**, 405 (2015); https://doi.org/10.2298/HEMIND140330057R
10. M.A. Abdelgawad et al., *Bioorg. Chem.*, **107**, 104558 (2021); https://doi.org/10.1016/j.bioorg.2020.104558
11. A. EL Mansouri, A. Oubella, A. Mehdi, M.Y. AitItto, M. Zahouily, H. Morjani and H.B. Lazrek, *Eur. J. Med. Chem.*, **85**, 245 (2014); https://doi.org/10.1016/j.ejmech.2014.07.103
12. N.K. Salam, T.H. Huang, B.P. Kota, M.S. Kim, Y. Li and D.E. Hibbs, *Chem. Biol. Drug Des.*, **71**, 57 (2008); https://doi.org/10.1111/j.1747-0285.2007.00606.x

13. P.R. Krishnendu, S. Benny, S. Kumar, J. Jayan, V. Bhaskar, L.K. Pappachen, T.P. Aneesh, M.A. Abdelgawad, M.M. Ghoneim, O. Nicolotti, S.M. Zachariah and B. Mathew, *J. Mol. Struct.*, **1295**, 136634 (2024); https://doi.org/10.1016/j.molstruc.2023.136634
14. A. Raju and D.B. Yadav, *J. Pharm. Res.*, **9**, 15 (2015).
15. R.S. Keri, M.R. Patil, S.A. Patil and S. Budagumpi, *Eur. J. Med. Chem.*, **89**, 207 (2015); https://doi.org/10.1016/j.ejmech.2014.10.059
16. M.L. Bolognesi and A. Cavalli, *ChemMedChem*, **11**, 1190 (2016); https://doi.org/10.1002/cmdc.201600161
17. E. Lionta, G. Spyrou, D.K. Vassilatis and Z. Cournia, *Curr. Top. Med. Chem.*, **14**, 1923 (2014); https://doi.org/10.2174/1568026614666140929124445
18. R.G. Parr and W. Yang, (1995). Density-Functional Theory of Atoms and Molecules. Oxford University Press.
19. M.J. Frisch, G.W. Trucks, H.B. Schlegel, G E. Scuseria, M.A. Robb, J.R. Cheeseman, G. Scalmani, V. Barone, B. Mennucci, G.A. Petersson, H. Nakatsuji, M. Caricato, X. Li, H.P. Hratchian, A.F. Izmaylov, J. Bloino, G. Zheng, J.L. Sonnenberg, M. Hada, M. Ehara, K. Toyota, R. Fukuda, J. Hasegawa, M. Ishida, T. Nakajima, Y. Honda, O. Kitao, H. Nakai, T. Vreven, J.A. Montgomery Jr., J.E. Peralta, F. Ogliaro, M. Bearpark, J. J. Heyd, E. Brothers, K.N. Kudin, V. N. Staroverov, R. Kobayashi, J. Normand, K. Raghavachari, A. Rendell, J.C. Burant, S.S. Iyengar, J. Tomasi, M. Cossi, N. Rega, J.M. Millam, M. Klene, J.E. Knox, J.B. Cross, V. Bakken, C. Adamo, J. Jaramillo, R. Gomperts, R. E. Stratmann, O. Yazyev, A J. Austin, R. Cammi, C. Pomelli, J. W. Ochterski, R. L. Martin, K. Morokuma, V.G. Zakrzewski, G.A. Voth, P. Salvador, J.J. Dannenberg, S. Dapprich, A. D. Daniels, O. Farkas, J.B. Foresman, J.V. Ortiz, J. Cioslowski and D.J. Fox, Gaussian 09, Revision E.01, Gaussian, Inc., Wallingford, CT, USA (2016).
20. A.D. McLean and G.S. Chandler, *J. Chem. Phys.*, **72**, 5639 (1980); https://doi.org/10.1063/1.438980
21. R. Krishnan, J.S. Binkley, R. Seeger and J.A. Pople, *J. Chem. Phys.*, **72**, 650 (1980); https://doi.org/10.1063/1.438955
22. R.C. Binning Jr. and L.A. Curtiss, *J. Comput. Chem.*, **11**, 1206 (1990); https://doi.org/10.1002/jcc.540111013
23. R.K. Dennington, T.A. Keith and J.M. Millam, GaussView 6.0, Semichem Inc., Shawnee Mission, KS, USA (2016).
24. G.A. Zhurko, Chemcraft-Graphical Software for Visualization of Quantum Chemistry Computations, version 1.8, build 682 (2020).
25. M.H. Jamroz, *Spectrochim. Acta A Mol. Biomol. Spectrosc.*, **114**, 220 (2013); https://doi.org/10.1016/j.saa.2013.05.096
26. T. Lu and F. Chen, *J. Comput. Chem.*, **33**, 580 (2012); https://doi.org/10.1002/jcc.22885
27. A. Daina, O. Michielin and V. Zoete, *Sci. Rep.*, **7**, 42717 (2017); https://doi.org/10.1038/srep42717
28. R.A. Laskowski, *Bioinformatics*, **23**, 1824 (2007); https://doi.org/10.1093/bioinformatics/btm085
29. D.E.V. Pires, T.L. Blundell and D.B. Ascher, *J. Med. Chem.*, **58**, 4066 (2015); https://doi.org/10.1021/acs.jmedchem.5b00104
30. M.J. Lucido, B.J. Orlando, A.J. Vecchio and M.G. Malkowski, *Biochemistry*, **55**, 1226 (2016); https://doi.org/10.1021/acs.biochem.5b01378
31. The Pymol Molecular Graphics System, Version 1.8 Schrodinger, LLC.
32. G.M. Morris, R. Huey, W. Lindstrom, M.F. Sanner, R.K. Belew, D.S. Goodsell and A.J. Olson, *J. Comput. Chem.*, **30**, 2785 (2009); https://doi.org/10.1002/jcc.21256
33. D. Sahin, R.A. Kepekci, M. Feizi-Dehnayebi, S. Akkoc, J.V. Cuevas-Vicario and N. Micale, *ChemistrySelect*, **9**, e202304572 (2024); https://doi.org/10.1002/slct.202304572
34. BIOVIA, Dassault Systèmes, Discovery Studio Visualizer, version 21.1.0.20298, San Diego, CA, USA: Dassault Systèmes (2020).
35. M.J. Abraham, T. Murtola, R. Schulz, S. Páll, J.C. Smith, B. Hess and E. Lindahl, *SoftwareX*, **1–2**, 19 (2015); https://doi.org/10.1016/j.softx.2015.06.001
36. J. Huang and A.D. MacKerell Jr., *J. Comput. Chem.*, **34**, 2135 (2013); https://doi.org/10.1002/jcc.23354
37. M. Bugnon, M. Goullieux, U.F. Röhrig, M.A.S. Perez, A. Daina, O. Michielin and V. Zoete, *J. Chem. Inf. Model.*, **63**, 6469 (2023); https://doi.org/10.1021/acs.jcim.3c01053
38. M.S. Valdés-Tresanco, M.E. Valdés-Tresanco, P.A. Valiente and E. Moreno, *J. Chem. Theory Comput.*, **17**, 6281 (2021); https://doi.org/10.1021/acs.jctc.1c00645
39. R.A. Shinde, V.A. Adole and B.S. Jagdale, *Vietnam J. Chem.*, **59**, 800 (2021); https://doi.org/10.1002/vjch.202100028
40. D. Villaño, M.S. Fernández-Pachón, M.L. Moyá, A.M. Troncoso and M.C. García-Parrilla, *Talanta*, **71**, 230 (2007); https://doi.org/10.1016/j.talanta.2006.03.050
41. M.P. Andersson and P. Uvdal, *J. Phys. Chem. A*, **109**, 2937 (2005); https://doi.org/10.1021/jp045733a
42. G. Socrates, Infrared and Raman Characteristic Group Frequencies: Tables and Charts, Chichester, U.K.: John Wiley & Sons, edn 3 (2010).
43. D. Lin-Vien, The Handbook of Infrared and Raman Characteristic Frequencies of Organic Molecules, Academic Press (1991).
44. M. Tammer, *Colloid Polym. Sci.*, **283**, 235 (2004); https://doi.org/10.1007/s00396-004-1164-6
45. I.H. Joe, G. Aruldhas, S. Anbukumar and P. Ramasamy, *Cryst. Res. Technol.*, **29**, 685 (1994); https://doi.org/10.1002/crat.2170290520
46. G. Varsányi and L. Láng, Assignments for Vibrational Spectra of Seven Hundred Benzene Derivatives, Wiley: New York (1974).
47. A.J. Abkowicz-Bieńko, Z. Latajka, D.C. Bieńko and D. Michalska, *Chem. Phys.*, **250**, 123 (1999); https://doi.org/10.1016/S0301-0104(99)00296-7
48. N. Sundaraganesan, S. Illakiamani, C. Meganathan and B.D. Joshua, *Spectrochim. Acta A Mol. Biomol. Spectrosc.*, **67**, 214 (2007); https://doi.org/10.1016/j.saa.2006.07.004
49. M. Karabacak, M. Cinar, A. Poiyamozhi N. Sundaraganesan and M. Kurt, *Spectrochim. Acta A Mol. Biomol. Spectrosc.*, **117**, 234 (2014); https://doi.org/10.1016/j.saa.2013.07.095
50. M. Karabacak, M. Kurt, M. Çınar and A. Çoruh, *Mol. Phys.*, **107**, 253 (2009); https://doi.org/10.1080/00268970902821579
51. A. Bendjeddou, T. Abbaz, A. Gouasmia and D. Villemin, *Int. Res. J. Pure Appl. Chem.*, **12**, 1 (2016); https://doi.org/10.9734/IRJPAC/2016/27066
52. R.G. Parr and W. Yang, Functional Theory of Atoms and Molecules, Oxford University Press: New York (1989).
53. R. Ayers and P.W. Parr, *J. Am. Chem. Soc.*, **122**, 2010 (2000); https://doi.org/10.1021/ja9924039
54. A.E. Reed and F. Weinhold, *J. Chem. Phys.*, **83**, 1736 (1985); https://doi.org/10.1063/1.449360
55. M. Cossi, V. Barone, B. Mennucci and J. Tomasi, *Chem. Phys. Lett.*, **286**, 253 (1998); https://doi.org/10.1016/S0009-2614(98)00106-7
56. R.E. Stratmann, G.E. Scuseria and M.J. Frisch, *J. Chem. Phys.*, **109**, 8218 (1998); https://doi.org/10.1063/1.477483
57. A. Dreuw and M. Head-Gordon, *Chem. Rev.*, **105**, 4009 (2005); https://doi.org/10.1021/cr0505627
58. T. Etienne, X. Assfeld and A. Monari, *J. Chem. Theory Comput.*, **10**, 3896 (2014); https://doi.org/10.1021/ct5003994
59. T. Lu and F. Chen, *J. Comput. Chem.*, **33**, 580 (2012); https://doi.org/10.1002/jcc.22885
60. F. Plasser and H. Lischka, *J. Chem. Theory Comput.*, **8**, 2777 (2012); https://doi.org/10.1021/ct300307c
61. R. David, C. Daul and U. Heinemeyer, *Chem. Phys.*, **259**, 199 (2000).
62. F.N. Ajeel and A. Ahmed, *J. Mol. Model.*, **29**, 145 (2023); https://doi.org/10.1007/s00894-023-05545-0
63. H. Jacobsen, *Can. J. Chem.*, **86**, 695 (2008); https://doi.org/10.1139/v08-052
64. E.R. Johnson, S. Keinan, P. Mori-Sánchez, J. Contreras-García, A.J. Cohen and W. Yang, *J. Am. Chem. Soc.*, **132**, 6498 (2010); https://doi.org/10.1021/ja100936w
65. C.A. Lipinski, F. Lombardo, B.W. Dominy and P.J. Feeney, *Adv. Drug Deliv. Rev.*, **46**, 3 (2001); https://doi.org/10.1016/S0169-409X(00)00129-0
66. C.A. Lipinski, F. Lombardo, B.W. Dominy and P.J. Feeney, *Adv. Drug Del. Rev.*, **23**, 3 (1997); https://doi.org/10.1016/S0169-409X(96)00423-1
67. W.M. Pardridge, *J. Cereb. Blood Flow Metab.*, **32**, 1959 (2012); https://doi.org/10.1038/jcbfm.2012.126

68. U.M. Zanger and M. Schwab, *Pharmacol. Ther.*, **138**, 103 (2013); https://doi.org/10.1016/j.pharmthera.2012.12.007
69. S.K. Nigam and V. Bhatnagar, *Clin. Pharmacol. Ther.*, **94**, 27 (2013); https://doi.org/10.1038/clpt.2013.82
70. OECD, *OECD Series on Testing and Assessment*, (2021); https://doi.org/10.1787/0ed2abf5-en
71. F. Fitzpatrick, *Curr. Pharm. Des.*, **10**, 577 (2004); https://doi.org/10.2174/1381612043453144
72. A.L. Blobaum and L.J. Marnett, *J. Med. Chem.*, **50**, 1425 (2007); https://doi.org/10.1021/jm0613166
73. S.A. Hollingsworth and P.A. Karplus, *Biomol. Concepts*, **1**, 271 (2010); https://doi.org/10.1515/bmc.2010.022
74. Z. Sadeghian, M. Bayat and D. Gheidari, *Nanoscale Adv.*, **7**, 5760 (2025); https://doi.org/10.1039/D5NA00182J
75. D. Gheidari, M. Mehrdad and M. Bayat, *Sci. Rep.*, **14**, 3084 (2024); https://doi.org/10.1038/s41598-024-53514-1
76. E. Durham, B. Dorr, N. Woetzel, R. Staritzbichler and J. Meiler, *J. Mol. Model.*, **15**, 1093 (2009); https://doi.org/10.1007/s00894-009-0454-9
77. K. Karunakaran and R. Muniyan, *J. Biomol. Struct. Dyn.*, **43**, 1893 (2025); https://doi.org/10.1080/07391102.2023.2293265
78. Y.-X. Zhu, Y.-J. Sheng, Y.-Q. Ma and H.-M. Ding, *J. Phys. Chem. B*, **126**, 1700 (2022); https://doi.org/10.1021/acs.jpcb.1c09424
79. A.W. Bauer, W.M.M. Kirby, J.C. Sherris and M. Turck, *Am. J. Clin. Pathol.*, **45(4_ts)**, 493 (1966); https://doi.org/10.1093/ajcp/45.4_ts.493
80. Clinical and Laboratory Standards Institute (CLSI), Performance Standards for Antimicrobial Susceptibility Testing, CLSI supplement M100. Wayne, PA, USA: Clinical and Laboratory Standards Institute, edn 31 (2021).
81. Clinical and Laboratory Standards Institute (CLSI), Reference Method for Broth Dilution Antifungal Susceptibility Testing of Filamentous Fungi; Approved Standard, CLSI document M38-A2, vol. 28, no. 16. Wayne, PA, USA: Clinical and Laboratory Standards Institute (2008).
82. W. Brand-Williams, M.E. Cuvelier and C. Berset, *Lebensm. Wiss. Technol.*, **28**, 25 (1995); https://doi.org/10.1016/S0023-6438(95)80008-5